IOP Publishing Journal of Physics B: Atomic, Molecular and Optical Physics

J. Phys. B: At. Mol. Opt. Phys. **54** (2021) 144001 (9pp) https://doi.org/10.1088/1361-6455/ac0d3e

Influence of nonadiabatic, nondipole and quantum effects on the attoclock signal

Yongzhe Ma[1], Jinyu Zhou[2], Peifen Lu[1], Hongcheng Ni[1,3,*] and Jian Wu[1,3,4]

[1] State Key Laboratory of Precision Spectroscopy, East China Normal University, Shanghai 200241, People's Republic of China
[2] School of Physics and Electronic Science, East China Normal University, Shanghai 200241, People's Republic of China
[3] NYU-ECNU Joint Institute of Physics, New York University at Shanghai, Shanghai 200062, People's Republic of China
[4] Collaborative Innovation Center of Extreme Optics, Shanxi University, Taiyuan, Shanxi 030006, People's Republic of China

E-mail: hcni@lps.ecnu.edu.cn and jwu@phy.ecnu.edu.cn

Received 26 May 2021, revised 14 June 2021
Accepted for publication 20 June 2021
Published 5 August 2021

Abstract

The attoclock is an important tool offering the capability to time resolve tunneling ionization. In this article, we systematically study the influence of nonadiabatic, nondipole and quantum effects on the attoclock signal. In contrast to previous studies, where a single peak offset angle is used to represent the attoclock information, we survey the whole momentum distribution of the attoclock signal. We find that nonadiabaticity affects the overall momentum distribution, the quantum effect of intercycle interference changes substantially the attoclock offset angle, and the nondipole effect plays a negligible role in the attoclock signal in the polarization plane. The present study is essential for a quantitatively correct interpretation of the attoclock experimental results.

Keywords: attoclock, attoclock signal, attoclock offset angle, nonadiabatic effect, nondipole effect, quantum effect, intercycle interference

(Some figures may appear in colour only in the online journal)

1. Introduction

The problem of tunneling time has long been a topic of controversy in strong-field physics [1]. With advances in the laser technology, ultra-short intense laser pulses become routinely available, facilitating the development of the attoclock technique [2], which can be employed to measure the tunneling time [3–7], or, more precisely, the time the electron appears at the tunnel exit relative to the peak of the laser field. This technique utilizes a strong elliptically polarized laser pulse, where the rotating vector potential maps the tunneling time to the photoelectron deflection angle in the polarization plane. Up to date, the interpretation of the attoclock results has been limited to the single integrated value of the attoclock offset angle, which is typically chosen as the peak or average angle in the polarization plane [8–12]. Among other problems, it was argued that the offset angle indeed varies at different radial momenta of the attoclock signal [7, 13–17], which poses the question how useful a single value of the offset angle is to interpret the attoclock results. In this article, we evaluate additionally the entire momentum distribution of the attoclock signal, and systematically study the influence of different factors, including nonadiabatic, nondipole and intercycle quantum interference effects, on the attoclock signal, which is essential for a quantitatively correct interpretation of the attoclock experimental results.

For any system with a time-dependent Hamiltonian, the energy is not conserved. Contrary to a pure tunneling

* Author to whom any correspondence should be addressed.

 © 2021 IOP Publishing Ltd Printed in the UK

process with a particle impinging onto a static potential, the process of tunneling ionization is induced by a time-varying intense infrared laser pulse, making tunneling ionization inherently nonadiabatic. The nonadiabatic tunneling effect has been known to induce energy variations across the tunneling barrier [16], shifts of the central transverse tunneling momentum [17, 18], interplay with orbital angular momentum [19, 20] and coupling to the nondipole effects on the subcycle time scale [21]. Importantly, it was found, based on the same attoclock signal, that whether there is a tunneling time delay depends on whether nonadiabaticity is fully and consistently accounted for [22, 23].

The attoclock results have so far been interpreted under the assumption of dipole approximation, in which condition the laser pulse transfers only energy but not momentum. With the advancements in the detecting technology, the small momentum transfer from the laser field to the departing electron becomes accessible [24]. Recently, the attoclock technique has been applied to resolve the linear momentum transfer on the subcycle level beyond the dipole approximation [21, 25]. Here, the nondipole effect has been time resolved with the attoclock angle in the polarization plane. However, the reverse action, namely the influence of the nondipole effect on the attoclock signal, including the attoclock offset angle, has not been quantified.

In a multicycle attoclock laser pulse, the intercycle interference effect would undoubtedly alter the attoclock signal. However, to what extent it would affect the interpretation of the attoclock results remains unclear. In addition, the transition amplitude could generally be broken down into the exponential part, the prefactor and the Jacobian factor. How each factor plays a role also remains unclear so far.

In this article, we systematically study the influence of nonadiabatic, nondipole, quantum interference effects and different factors in the tunneling rate on the attoclock signal. In order to consistently study the influence of different factors, we establish the results from the solution of time-dependent Shrödinger equation (TDSE) as the standard accurate attoclock momentum distribution, and results considering different factors can compare to the standard distribution. The results considering different factors are obtained using trajectory-based simulations, including the classical-trajectory Monte Carlo (CTMC) method, the quantum-trajectory Monte Carlo (QTMC) method [26] and the semiclassical two-step (SCTS) model [27]. Under this framework, the quantum effect can be studied by comparing results obtained with CTMC to QTMC/SCTS, the nonadiabatic effect can be studied by comparing results starting from different initial tunneling conditions where nonadiabaticity can be switched on and off, and the nondipole effect can be studied by altering the Newtonian equation of motion to evolve the trajectories. To make the comparison, we take advantage of the entire information of the attoclock signal based on the whole final momentum distribution. To this end, we apply three techniques, including calculating the overlap [22], the Shannon entropy difference (SED) [28, 29] and the Kullback–Leibler divergence (KLD) [30], with respect to the TDSE solution.

This paper is organized as follows. In section 2, we present the theoretical methods used, including the methods to compute the attoclock momentum distribution (TDSE, CTMC, QTMC and SCTS), different initial conditions with or without nonadiabaticity, and methods for comparing the entire distribution (overlap, SED and KLD). In section 3, we study the influence of different factors on the attoclock signal. The article ends with a summary given in section 4. Atomic units are used throughout the article unless stated otherwise.

2. Theoretical methods

In this section, we briefly describe the main theoretical methods used in the present study, including the simulation methods, various initial conditions, and comparison methods.

2.1. Simulation methods

In order to study the influence of intercycle interference effect on the attoclock signal, we carry out trajectory-based simulations including CTMC, QTMC and SCTS, and compare to the results of TDSE simulations, which is regarded as the accurate result in this study.

2.1.1. Time-dependent Schrödinger equation. In an intense laser field, the electronic wave function $\Psi(\boldsymbol{r}, t)$ evolves according to TDSE as

$$i\frac{\partial}{\partial t}\Psi(\boldsymbol{r}, t) = \left\{\frac{1}{2}[\boldsymbol{p} + \boldsymbol{A}(t)]^2 + V(r)\right\}\Psi(\boldsymbol{r}, t), \tag{1}$$

where $\boldsymbol{p}$ is the momentum operator, $\boldsymbol{A}(t)$ is the laser vector potential in the form of

$$\boldsymbol{A}(t) = \frac{A_0}{\sqrt{1+\epsilon^2}}\cos^4\left(\frac{\omega t}{2N}\right)\begin{pmatrix}\cos(\omega t)\\ \epsilon\,\sin(\omega t)\end{pmatrix}, \tag{2}$$

with A_0 the amplitude of the vector potential, ϵ the ellipticity, ω the central angular frequency, N the total number of laser periods, and

$$V(r) = -\frac{1+\exp(-r^2/2)}{\sqrt{r^2+a}} \tag{3}$$

is the single-active-electron atomic potential with the soft-core parameter $a = 0.836$ tuned to match the ionization potential of the helium atom. The TDSE simulation is carried out on a two-dimensional grid with a grid step of $\Delta x = 0.2$ and 8192 grid points in each direction, and a time step of $\Delta t = 0.02$. The ground-state wave function is obtained by the imaginary time propagation method and the propagation of the wave function in the laser field is carried out using the split-operator Fourier method. An absorber of the form $1/[1+\exp\{(r-r_0)/d\}]$, where $r_0 = 804.2$ and $d = 4$, is placed around the center of the simulation box to damp the outgoing wave packet in order to avoid reflections from the grid border. The attoclock momentum distribution is obtained by accumulatively projecting the absorbed wave function onto the Volkov state at each time step [31, 32].

2.1.2. CTMC method. The CTMC method is a great implementation of the continuum propagation part of the classic two-step and three-step model. It disregards all quantum effects but takes full account of the Coulomb potential during the continuum motion of the electron. It applies whenever the quantum effect plays a minor role but the Coulomb interaction is important, such as in the simulation of nonsequential double ionization. In the current setting, it acts as a good counterpart for studying the influence of interference effects after tunneling by completely neglecting quantum information. Here, the electron is guided by the combined interaction of the laser field and the Coulomb potential, and the trajectory can be solved by the Newtonian equation of motion:

$$\ddot{\boldsymbol{r}} = -\boldsymbol{F}(t) - \nabla V(r), \tag{4}$$

where $\boldsymbol{F}(t) = -\dot{\boldsymbol{A}}(t)$ is the laser electric field. Using the attoclock pulse, the electrons no longer return to the nucleus. After the laser pulse ends, the Kepler formula [33] is used to obtain the asymptotic momentum and the trajectories with similar ending momenta are binned in a small momentum box to produce the final momentum distribution.

2.1.3. QTMC method. The QTMC method utilizes the same underlying classical trajectories as in CTMC, but tags each trajectory with a phase accumulated during its continuum excursion [26]:

$$\Phi = -\int_{t_0}^{\infty} \left\{ \frac{v(t)^2}{2} + V[r(t)] + I_\mathrm{p} \right\} \mathrm{d}t, \tag{5}$$

where t_0 is the tunneling exit time, or the time of launch. Trajectories with similar ending momenta are binned with coherent summation of the probability amplitude.

2.1.4. SCTS model. SCTS improves the phase for the trajectory in QTMC [27], with

$$\Phi = -\boldsymbol{v}_0 \cdot \boldsymbol{r} - \int_{t_0}^{\infty} \left\{ \frac{v(t)^2}{2} + V[r(t)] - \boldsymbol{r} \cdot \nabla V[r(t)] + I_\mathrm{p} \right\} \mathrm{d}t. \tag{6}$$

There are two differences between equations (5) and (6). Firstly, in QTMC, equation (5) is derived under quasi-static conditions, the initial longitudinal velocity is zero so the term $-\boldsymbol{v}_0 \cdot \boldsymbol{r}$ vanishes. Secondly, SCTS has one more term than QTMC in the integrand originating from the equation of motion.

2.2. Different initial conditions and ionization rates

The trajectory-based methods launch classical electron trajectories starting with a certain set of initial conditions. The initial conditions can be chosen to include, partially include, or exclude nonadiabatic tunneling effects, thus enabling a study of the influence of nonadiabaticity in the attoclock signal. Following we present various ways to sample the initial conditions.

2.2.1. Strong-field approximation. The strong-field approximation (SFA) [34–36] is a commonly used theoretical method when studying the interaction of lasers with atoms and molecules. Its key idea is to use the Volkov state, which is the eigenstate of an electron solely in the laser field, to describe the final continuum state of electrons, and use discrete eigenstates that are not disturbed by the laser to describe the initial bound state. As a result, the transition amplitude between an atomic bound state and the continuum state with photoelectron asymptotic momentum $\boldsymbol{p}$ is given by

$$M_{\boldsymbol{p}} = -i \int_{-\infty}^{+\infty} \langle \Psi_{\boldsymbol{p}} | \boldsymbol{r} \cdot \boldsymbol{F}(t) | \Psi_0 \rangle \mathrm{d}t, \tag{7}$$

where $\Psi_0(\boldsymbol{r}, t) = \psi_0(\boldsymbol{r}) \mathrm{e}^{\mathrm{i} I_\mathrm{p} t}$ is the initial bound state wave function unperturbed by the laser field with I_p standing for the ionization potential and $\Psi_{\boldsymbol{p}}(\boldsymbol{r}, t) = \exp\left\{ i[\boldsymbol{p} + \boldsymbol{A}(t)] \cdot \boldsymbol{r} - \frac{i}{2}\int^t [\boldsymbol{p} + \boldsymbol{A}(t')]^2 \mathrm{d}t' \right\}$ is the Volkov state (in the length gauge).

The SFA gives the transition amplitude to a certain momentum $\boldsymbol{p}$. With a further saddle-point approximation [37, 38], it can be used as an accurate way to prepare initial conditions to launch classical electron trajectories. Specifically, saddle-point times t_s are identified according to the saddle-point equation

$$\frac{1}{2}[\boldsymbol{p} + \boldsymbol{A}(t_\mathrm{s})]^2 + I_\mathrm{p} = 0, \tag{8}$$

that contribute most to the integral (7), where $t_\mathrm{s} = t_\mathrm{r} + i t_\mathrm{i}$ must be a complex number to satisfy the saddle-point equation, with t_r the tunneling exit time and t_i relating to the ionization probability. Generally, for a certain set of laser and target parameters, the larger the t_i, the smaller the ionization probability. After taking care of the initial bound state as well, the modified SFA [39–41] gives (ignoring field-independent constants)

$$M_\mathrm{SFA} = \sum_{t_\mathrm{s}} \frac{\exp(-iS_\mathrm{s})}{\{[\boldsymbol{p} + \boldsymbol{A}(t_\mathrm{s})] \cdot \boldsymbol{F}(t_\mathrm{s})\}^{\alpha/2}}, \tag{9}$$

where $\alpha = 1 + Z/\sqrt{2I_\mathrm{p}}$ with Z the asymptotic ionic charge and

$$S_\mathrm{s} = \int_{t_\mathrm{s}}^{t_\mathrm{r}} \left\{ \frac{1}{2}[\boldsymbol{p} + \boldsymbol{A}(t)]^2 + I_\mathrm{p} \right\} \mathrm{d}t. \tag{10}$$

Note that the momentum at the tunnel exit $\boldsymbol{k}$ relates to the asymptotic momentum $\boldsymbol{p}$ by $\boldsymbol{k} = \boldsymbol{p} + \boldsymbol{A}(t_\mathrm{r})$, we can rewrite equation (9) as

$$M_\mathrm{SFA} = \sum_{t_\mathrm{s}} \frac{\exp(-iS_\mathrm{s})}{\{[\boldsymbol{k} - \boldsymbol{A}(t_\mathrm{r}) + \boldsymbol{A}(t_\mathrm{s})] \cdot \boldsymbol{F}(t_\mathrm{s})\}^{\alpha/2}}, \tag{11}$$

expressed as a function of the tunneling exit time t_r and the initial tunneling momentum $\boldsymbol{k}$, which can now be sampled over to launch trajectories with a (complex) weight corresponding to the transition amplitude. In addition, the tunneling exit position can be defined from

$$\boldsymbol{r}_\mathrm{SFA} = \mathrm{Re} \int_{t_\mathrm{s}}^{t_\mathrm{r}} [\boldsymbol{p} + \boldsymbol{A}(t)] \mathrm{d}t = \mathrm{Im} \int_0^{t_\mathrm{i}} \boldsymbol{A}(t_\mathrm{r} + it) \mathrm{d}t. \tag{12}$$

Note that nonadiabatic tunneling effects are fully included by using initial conditions prepared by SFA.

2.2.2. SFA with adiabatic expansion. In the case of a tunneling ionization process, we may expand the vector potential $\boldsymbol{A}(t_s)$ in terms of small t_i (or small Keldysh parameter γ corresponding to a tunneling scenario) up to the second order [23, 42]

$$\boldsymbol{A}(t_r + it_i) = \boldsymbol{A}(t_r) - it_i\boldsymbol{F}(t_r) + \frac{1}{2}t_i^2\dot{\boldsymbol{F}}(t_r) + O(t_i^3), \tag{13}$$

where $\dot{\boldsymbol{F}}(t_r) = \frac{d\boldsymbol{F}(t_r)}{dt_r}$. With such expansion, we obtain the tunneling rate, which we term as SFA with adiabatic expansion (SFAAE), as

$$W_{\mathrm{SFAAE}}(\boldsymbol{k}_\perp, \boldsymbol{F}) = \frac{\exp\left[-\frac{2(k_\perp^2+2I_p)^{3/2}}{3\sqrt{F^2-\boldsymbol{k}_\perp\cdot\dot{\boldsymbol{F}}}}\right]}{[(k_\perp^2+2I_p)(F^2-\boldsymbol{k}_\perp\cdot\dot{\boldsymbol{F}})]^{\alpha/2}}, \tag{14}$$

where $\boldsymbol{k}_\perp$ is the transverse momentum in the polarization plane, which, after such expansion, is perpendicular to the instantaneous electric field direction. The corresponding location of the tunnel exit is

$$r_{\mathrm{SFAAE}}(\boldsymbol{k}_\perp, \boldsymbol{F}) \approx -\frac{\boldsymbol{F}}{2}\frac{k_\perp^2+2I_p}{F^2-\boldsymbol{k}_\perp\cdot\dot{\boldsymbol{F}}}. \tag{15}$$

The SFAAE method takes the first three terms of the Taylor expansion of the vector potential $\boldsymbol{A}(t_s)$ and thus takes partial account for nonadiabaticity, which has been shown to very closely reproduce the SFA results [23]. This will also become clear later in this article. SFAAE has the advantage that the ionization rate can be written in an expression similar to the familiar Ammosov–Delone–Krainov (ADK) theory [43–45] (shown below) without the necessity to solve the saddle-point equation, which speeds up the calculation substantially.

2.2.3. ADK theory. The ionization rate in the ADK theory [43–45] can be written as

$$W_{\mathrm{ADK}}(k_\perp, F) = \frac{\exp\left[-\frac{2(k_\perp^2+2I_p)^{3/2}}{3F}\right]}{[(k_\perp^2+2I_p)F^2]^{\alpha/2}}. \tag{16}$$

It is expressed in a form different from what is often used in the literature in two ways: (i) the prefactor is different that considers $k_\perp$ and an exponent of α. We have intentionally used this form so that it aligns better with previous SFA and SFAAE methods for the sake of comparison. We note that using a typical ADK prefactor does not change our conclusion below. (ii) The exponent in the numerator is expressed differently. To retrieve the normal ADK expression, we could expand it in terms of $k_\perp$: $\exp[-2(k_\perp^2+2I_p)^{3/2}/3F] \approx \exp[-2(2I_p)^{3/2}/3F]\exp(-\sqrt{2I_p}k_\perp^2/F)$.

The location of the tunnel exit is

$$\boldsymbol{r}_{\mathrm{ADK}}(k_\perp, \boldsymbol{F}) \approx -\frac{\boldsymbol{F}}{2}\frac{k_\perp^2+2I_p}{F^2}. \tag{17}$$

It is also different from the normally used I_p/F by taking $k_\perp$ into account. In this way, there is precisely no energy variation across the tunneling barrier, corresponding to an adiabatic tunneling scenario [23]: $E_{\mathrm{ADK}} = k_\perp^2/2 + \boldsymbol{r}_{\mathrm{ADK}}\cdot\boldsymbol{F} = -I_p$.

From the comparison to the SFAAE (14), the ADK equations presented here is clearly a limit of SFAAE with $\dot{\boldsymbol{F}} \to \boldsymbol{0}$, which thus is the adiabatic limit of the SFAAE (or SFA) theory.

2.3. Comparison methods

With different simulation methods and initial conditions, we may obtain the attoclock momentum distribution from various combinations, which can be compared to the accurate TDSE solution. Below we present different methods to compare the whole momentum distributions.

2.3.1. The overlap. The electron momentum spectra obtained by the simulations under similar initial conditions are generally quite close to each other. In order to compare two momentum distributions, we may calculate the overlap between them [22]

$$\mathrm{Overlap} = \frac{\int \mathrm{d}\boldsymbol{p}|\widetilde{\Psi}(\boldsymbol{p},t)|\sqrt{\rho(\boldsymbol{p},t)}}{\int \mathrm{d}\boldsymbol{p}|\widetilde{\Psi}(\boldsymbol{p},t)|^2}, \tag{18}$$

where $\rho(\boldsymbol{p},t)$ represents the momentum distribution obtained with various methods and $\widetilde{\Psi}(\boldsymbol{p},t)$ is the final momentum-space wave function from the TDSE simulation such that $|\widetilde{\Psi}(\boldsymbol{p},t)|^2$ is the corresponding momentum distribution regarded as the standard accurate solution. Clearly, overlap $\in [0, 1]$. The more similar the distribution is to the TDSE solution, the larger the value of overlap is.

2.3.2. The SED. Shannon borrowed the concept of entropy in thermodynamics, and defined the average amount of information in a message after excluding redundancy as 'information entropy' (thereafter called the Shannon entropy) [28, 29]

$$S = -\int \mathrm{d}\boldsymbol{p}\,\rho(\boldsymbol{p},t)\log[\rho(\boldsymbol{p},t)], \tag{19}$$

which uses a single value to represent the amount of information contained in the momentum distribution $\rho(\boldsymbol{p},t)$. This value can be compared to that calculated using the momentum distribution from the TDSE solution $|\widetilde{\Psi}(\boldsymbol{p},t)|^2$. We name the difference in them the SED ΔS. The more similar the distribution is to the TDSE solution, the smaller the value of SED ΔS is.

2.3.3. The KLD. The KLD (also called the relative entropy) [30] is a measure of the 'distance' between two probability distributions that is often used in computer vision

$$\mathrm{KLD} = -\int \mathrm{d}\boldsymbol{p}\,|\widetilde{\Psi}(\boldsymbol{p},t)|^2\,\log\left[\frac{|\widetilde{\Psi}(\boldsymbol{p},t)|^2}{\rho(\boldsymbol{p},t)}\right]. \tag{20}$$

In analogue to SED, the more similar the distribution is to the TDSE solution, the smaller the value of KLD is.

3. Influence of different factors on the attoclock signal

In order to systematically study the influence of different factors on the attoclock signal, we identify the TDSE momentum

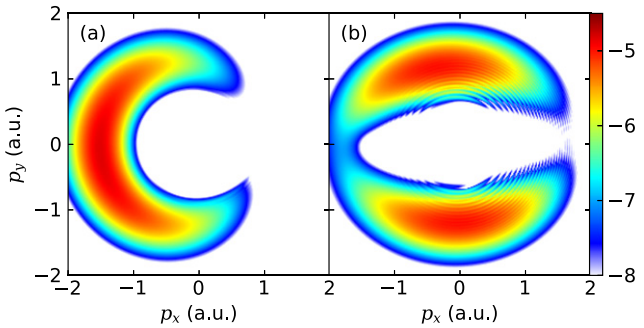

Figure 1. (a) The photoelectron momentum distribution (in logarithmic scale) of the helium atom with single active electron by solving TDSE, ionized by a two-cycle ($N = 2$) circularly polarized laser pulse at a wavelength of 800 nm and a peak intensity of 4.0×10^{14} W cm^{-2}. (b) Same as (a) but with a six-cycle ($N = 6$) elliptically polarized laser pulse with ellipticity $\epsilon = 0.75$.

distribution as the 'exact solution', which different methods may compare to. We employ the theoretical methods presented in the previous section to compare their respective results with TDSE to explore the influence of the nonadiabatic effect, quantum effect, tunneling ionization rate and nondipole effect on the attoclock signal. In this paper, we use 800 nm circularly polarized laser pulses with $N = 2$ or elliptically ($\epsilon = 0.75$) polarized laser pulses with $N = 6$ and a peak intensity of 4.0×10^{14} W cm^{-2}.

Figure 1(a) shows the photoelectron momentum distribution obtained by solving the TDSE under a short circularly polarized laser pulse with $N = 2$. For a long circularly polarized laser field, the momentum distribution would be a donut-shaped ring. For the present case of a short two-cycle laser pulse, the tunneling probability maximizes at the laser peak, around which the ionization probability drops substantially, resulting in an arc-shaped structure. For such a short pulse, the intercycle interference is missing. Take the $-x$-axis as the reference, the offset angle corresponding to the peak of the angular momentum distribution of the attoclock signal is 5.768°. Figure 1(b) is the photoelectron momentum distribution obtained by solving the TDSE under an elliptically polarized laser pulses with $\epsilon = 0.75$ and $N = 6$. Here, intercycle interference leads to the appearance of interference fringes. In an elliptically polarized multicycle laser pulse, the photoelectron momentum distribution is distributed along the minor axis of the polarization ellipse. For a short pulse of $N = 6$, the field envelope causes an asymmetry in the momentum distribution along the $+y$ and $-y$ directions. Take the $+y$-axis as the reference, the offset angles corresponding to the double peaks of the angular distribution of the attoclock signal are 15.215° and 178.908° respectively.

3.1. Influence of nonadiabatic effects

In order to explore the influence of nonadiabatic effects on the attoclock signal, we apply the initial conditions prepared by the SFA, SFAAE and ADK theories to perform trajectory-based numerical simulations using CTMC, QTMC and SCTS, where the Coulomb potential is taken full account for, as shown in figure 2. The laser parameters are the same as in figure 1(a).

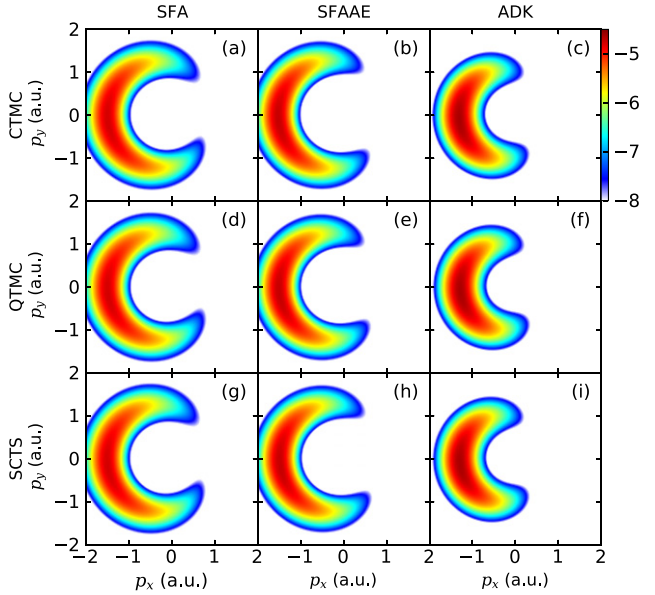

Figure 2. The attoclock signal (in logarithmic scale) obtained with different simulation methods and initial conditions. The simulation methods used in the first to the third rows are CTMC, QTMC and SCTS, and the initial conditions in the first to the third columns are given by the SFA, SFAAE and ADK theories, respectively. The same laser parameters are used as in figure 1(a).

Different rows in figure 2 corresponds to simulations performed with CTMC, QTMC and SCTS, respectively. For a two-cycle laser pulse, essentially only one cycle leads to discernible ionization, and intercycle interference is effectively missing, leading to the great similarity between the attoclock results for different rows.

Different columns in figure 2 corresponds to initial conditions prepared by SFA, SFAAE and ADK theories, respectively. In the ADK theory, the adiabatic approximation is adopted. The transverse momentum of the electron at the tunnel exit is a Gaussian distribution centered at zero, and the longitudinal momentum is set to be zero, which results in a narrower and smaller arc in the photoelectron momentum distribution than other scenarios. In contrast, the SFA theory does not employ the adiabatic approximation. The initial conditions obtained by solving the saddle-point equation fully include the nonadiabatic tunneling effect, so it is more similar to the attoclock signal obtained by solving the TDSE. SFAAE takes the first three terms of the Taylor expansion of the laser vector potential, which includes the majority of the nonadiabatic effects. It can also more or less match the attoclock signal obtained by solving the TDSE.

In order to quantitatively analyze the difference between the attoclock signal of different methods and initial conditions, the methods of overlap, SED, and KLD are used to compare different attoclock signals with that obtained by TDSE, as shown in table 1. It can be found that the overlaps of SFA and SFAAE to TDSE are not only greater than ADK, but also much closer to 1, and their SED and KLD are also smaller than ADK. This shows that the attoclock signal obtained by SFA and SFAAE are in good overall agreement with that obtained by solving TDSE. In addition, the data of SFA and SFAAE

Table 1. The similarity matrix between the attoclock signals obtained with different simulation methods (CTMC, QTMC and SCTS) and initial conditions (prepared by SFA, SFAAE or ADK theories) to that of TDSE. Comparison methods include the overlap, SED and KLD, as well as the attoclock offset angle deviation $\Delta\theta$ with respect to TDSE. The same laser parameters are used as in figure 1(a).

		SED	KLD	Overlap	$\Delta\theta$ (°)
	SFA	0.155	0.016	0.997	−0.080
CTMC	SFAAE	0.302	0.043	0.993	−0.808
	ADK	0.632	1.487	0.786	−0.715
	SFA	0.156	0.017	0.997	0.208
QTMC	SFAAE	0.319	0.051	0.992	−0.237
	ADK	0.635	1.800	0.744	−0.121
	SFA	0.156	0.017	0.997	0.203
SCTS	SFAAE	0.319	0.051	0.992	−0.235
	ADK	0.635	1.800	0.744	−0.119

Table 2. The similarity matrix between the attoclock signals obtained with different simulation methods (CTMC, QTMC and SCTS) and initial conditions (prepared by SFA, SFAAE or ADK theories) to that of TDSE. Comparison methods include the overlap, SED and KLD, as well as the attoclock offset angle deviations $\Delta\theta_1$ and $\Delta\theta_2$ with respect to TDSE. The same laser parameters are used as in figure 1(b).

		SED	KLD	Overlap	$\Delta\theta_1$ (°)	$\Delta\theta_2$ (°)
	SFA	0.078	0.043	0.992	−2.094	1.769
CTMC	SFAAE	0.188	0.059	0.991	−0.416	−2.660
	ADK	0.455	0.631	0.906	0.072	−2.277
	SFA	0.170	0.035	0.994	−0.270	0.038
QTMC	SFAAE	0.246	0.045	0.993	−0.402	−1.647
	ADK	0.472	0.817	0.881	0.393	−1.419
	SFA	0.170	0.043	0.993	−0.278	0.030
SCTS	SFAAE	0.246	0.045	0.992	−0.402	−1.649
	ADK	0.472	0.817	0.881	0.392	−1.421

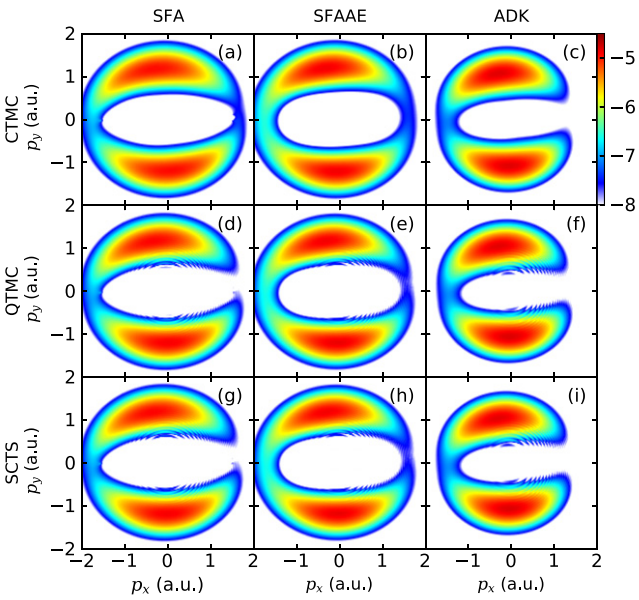

Figure 3. The attoclock signal (in logarithmic scale) obtained with different simulation methods and initial conditions. The simulation methods used in the first to the third rows are CTMC, QTMC and SCTS, and the initial conditions in the first to the third columns are given by the SFA, SFAAE and ADK theories, respectively. The same laser parameters are used as in figure 1(b).

are very close to each other, indicating a high degree of similarity between results obtained using the two methods. Both methods have their own advantages and disadvantages. SFA has a wider range of applicabilities, but it needs the solution of the saddle-point equation. SFAAE is only suitable for the tunneling scenario, but there is no need to solve the saddle-point equation. It comes with a form of ionization rate close to that of ADK, which greatly reduces the computation time compared to SFA but retains almost fully the nonadiabatic effects.

In addition to the overall signal distribution, the peak offset angles of the attoclock signals, as commonly done, are obtained by different methods and compared to that by solving TDSE, as also shown in table 1. The difference in the attoclock offset angle to the TDSE result is defined as $\Delta\theta$, the offset angle deviation. Generally, the deviation $\Delta\theta$ is smallest when the initial condition is prepared by SFA, indicating the importance of nonadiabaticity in the interpretation of the attoclock results.

Table 3. Influence of the prefactor and the Jacobian factor in the transition amplitude studied using SCTS–SFA compared to TDSE. The same laser parameters are used as in figure 1(a).

	SED	KLD	Overlap	$\Delta\theta$ (°)
Exp	0.157	0.217	0.964	0.285
Exp + pre	0.177	0.318	0.948	0.342
Exp + jac	0.136	0.015	0.998	0.129
Full	0.156	0.017	0.997	0.203

3.2. *Influence of quantum interference effects*

In order to explore the influence of intercycle quantum interference effects on the attoclock signal, we employ a longer elliptically polarized laser pulse with $N = 6$ and $\epsilon = 0.75$. Shown in figure 3 are attoclock signals obtained by different simulation methods (by row: CTMC, QTMC and SCTS) with initial conditions prepared by different theories (by column: SFA, SFAAE and ADK). Comparing the results obtained by QTMC/SCTS to that by CTMC, it is clear that QTMC and SCTS give rise to interference fringes similar to the TDSE results, because they have included the phase during the continuum excursion of the electron trajectories. In addition to the quantum effects illustrated by different rows, comparison of different columns again stresses the importance of inclusion of nonadiabaticity to obtain attoclock signals similar to TDSE, as has been clear from above.

A quantitative study by comparison of the overall momentum distributions obtained by different methods to that of TDSE, as shown in table 2, indicates that inclusion of quantum interference effects does not generally lead to an overall improvement of the attoclock signal other than the appearance of interference fringes. An additional comparison of the attoclock offset angle, however, shows that the intercycle interference leads to substantial changes in the attoclock angular

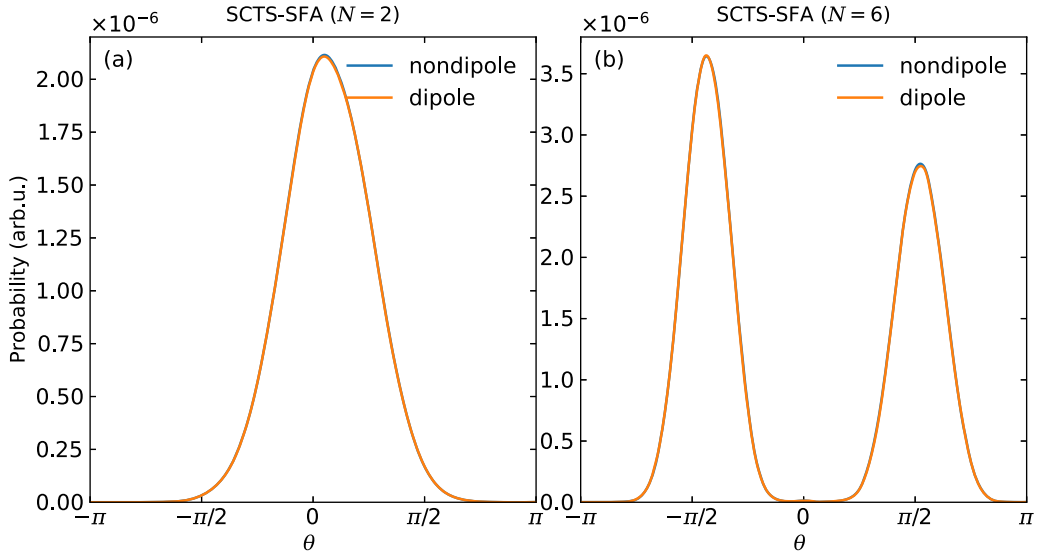

Figure 4. The attoclock photoelectron angular distribution with and without dipole approximation in the polarization plane with (a) two-cycle circularly polarized laser pulse as in figures 1(a) and (b) six-cycle elliptically polarized laser pulse as in figure 1(b).

distribution. Therefore, quantum interference is essential to obtain a correct attoclock offset angle. Previously, the attoclock signal is often obtained using CTMC simulations, which thus may lead to inaccurate calibration of the attoclock. Moreover, the comparison between SFA and SFAAE shows that it is important to include the phase of the transition amplitude in the weight of the electron trajectories to get an accurate offset angle, because the present implementation of SFAAE uses only the tunneling rate while SFA uses the complex transition amplitude which gives a much closer offset angle to TDSE.

3.3. Influence of tunneling rate

Through the analysis of the above two subsections, both QTMC–SFA and SCTS–SFA can give results similar to the 'exact solution' of TDSE. Here, we choose SCTS–SFA to study the effect of different forms of ionization amplitude on the attoclock signal. As shown in equation (9), the SFA transition amplitude or tunneling rate can in general be broken down into an exponential part (exp) and a prefactor (pre). When using the SFA method to solve the saddle-point equation, instead of searching for the saddle point directly for the attoclock momentum (p_x, p_y), we perform a coordinate transformation $(p_x, p_y) \to (t_\mathrm{r}, k_\perp)$ [21], where the release time t_r is chosen as the real part of the saddle-point time t_s and a momentum component is defined in the polarization plane

$$k_\perp = \frac{(\boldsymbol{p} + \mathrm{Re}\,\boldsymbol{A}(t_\mathrm{s})) \cdot (\mathrm{Im}\,A_y(t_\mathrm{s})\boldsymbol{e}_x - \mathrm{Im}\,A_x(t_\mathrm{s})\boldsymbol{e}_y)}{\sqrt{(\mathrm{Im}\,A_x(t_\mathrm{s}))^2 + (\mathrm{Im}\,A_y(t_\mathrm{s}))^2}}. \quad (21)$$

Within such a coordinate, the tunneling rate needs to include an additional Jacobian factor (jac).

As shown in table 3, we study the influence of the prefactor (pre) and the Jacobian factor (jac) by a comparison study which includes: (1) only the exponential part (exp); (2) the exponential part with prefactor (exp + pre); (3) the exponential part with Jacobian (exp + jac); (4) the full transition amplitude (full, or exp + pre + jac). From the data in table 3, it can be found that the different forms of the tunneling ionization amplitude do have a certain impact on the peak offset angle of the attoclock signal and the overall similarity. The results show that inclusion of the Jacobian factor is crucial, and the prefactor also leads to a somehow noticeable change.

3.4. Influence of nondipole effects

Three-dimensional trajectory simulations using Newtonian equation of motion under dipole approximation and without dipole approximation can be used to explore the impact of nondipole effects in the attoclock signal. In figure 4 we show the attoclock angular distributions using the SCTS model with initial conditions prepared by SFA with and without dipole approximation with (a) a two-cycle circularly polarized laser pulse and (b) a six-cycle elliptically polarized laser pulse. The curves with and without dipole approximation almost completely overlap. Therefore, the nondipole effect will not affect the attoclock angular distribution as well as the corresponding offset angle. Table 4 shows a quantitative study using different simulation methods and initial conditions, and the comparison data with and without dipole approximation are obtained for a two-cycle circularly polarized laser pulse. It can be seen that the SED and KLD between calculations done with and without dipole approximation are very small, and the overlap is close to 1, indicating that the nondipole effect plays a negligible role in altering the attoclock signal in the polarization plane. The results obtained for a six-cycle elliptically polarized laser pulse are similar and support the current conclusion.

This is indeed as expected. When there is no Coulomb potential, there is translation symmetry along the laser propagation direction, and thus the nondipole effect has no influence on the attoclock signal in the polarization plane. When the Coulomb potential is present, it would play a role in the momentum distribution in the polarization plane, which is however through coupling to the Coulomb potential, and thus

Table 4. Influence of the nondipole effects studied using different methods. Here, results with and without dipole approximation are compared with respect to each other. The same laser parameters are used as in figure 1(a).

		SED	KLD	Overlap	$\Delta\theta(^\circ)$
	SFA	−0.007 89	0.000 02	0.999 66	−0.020 75
CTMC	SFAAE	0.001 32	0.000 00	0.999 86	0.007 92
	ADK	0.001 71	0.000 00	0.999 74	0.007 72
	SFA	0.002 93	0.000 06	0.999 22	−0.018 20
QTMC	SFAAE	0.000 18	0.000 00	0.999 71	−0.004 34
	ADK	0.002 18	0.000 00	0.999 29	−0.014 38
	SFA	0.003 03	0.000 06	0.999 20	−0.017 74
SCTS	SFAAE	0.000 17	0.000 00	0.999 71	−0.003 96
	ADK	0.002 30	0.000 00	0.999 28	−0.016 16

is a higher order effect [21, 46], which, as shown here for the attoclock pulse, can be safely neglected.

4. Conclusion

The attoclock is widely used to time resolve the tunneling process and the calibration of time zero for attoclock is crucial for a quantitative interpretation of the signal. In this study, we systematically survey the influence of nonadiabatic, nondipole and quantum interference effects on the attoclock signal. In contrast to previous literature, where a single integrated value of the peak offset angle is used to represent the attoclock signal, we additionally take advantage of the full information provided by the entire attoclock momentum distribution where the overlap, SED and KLD are used as measures of similarity between different density distributions. With the present study, we make the following conclusions:

(a) Inclusion of nonadiabatic effects is essential for an overall agreement of the attoclock signal.
(b) Inclusion of intercycle quantum interference effects is crucial for a quantitatively correct attoclock offset angle.
(c) Inclusion of the phase of the transition amplitude in the weight of the electron trajectory is critical to obtain an accurate attoclock offset angle.
(d) Inclusion of the prefactor and Jacobian factor is important for an overall accurate attoclock signal.
(e) Nondipole effects play a negligible role in the attoclock signal in the polarization plane.

Based on these observations, a QTMC or SCTS simulation with initial conditions prepared by SFA and a weight containing the phase of the transition amplitude, which is essentially the trajectory-based Coulomb-corrected strong-field approximation (TCSFA) method [47–49], is the best combination up to now for a trajectory simulation to obtain an accurate attoclock signal. We note that most previous studies use CTMC simulations with ADK initial conditions and discard the initial phases, which thus may lead to quantitatively deficient interpretation of the attoclock results.

Acknowledgments

This work was supported by the National Key R & D Program of China (Grant Nos. 2018YFA0306303, 2019YFA0308300), the National Natural Science Fundation of China (Grant Nos. 11904103, 11834004, 91950203), the Science and Technology Commission of Shanghai Municipality (Grant Nos. 21ZR1420100, 19JC1412200, and a Major Project), and the Fundamental Research Funds for the Central Universities. Numerical computations were in part performed on the ECNU Multifunctional Platform for Innovation (001).

Data availability statement

The data that support the findings of this study are available upon reasonable request from the authors.

ORCID iDs

Hongcheng Ni https://orcid.org/0000-0003-4924-0921
Jian Wu https://orcid.org/0000-0002-1318-2291

References

[1] Landauer R and Martin T 1994 Barrier interaction time in tunneling *Rev. Mod. Phys.* **66** 217
[2] Eckle P, Smolarski M, Schlup P, Biegert J, Staudte A, Schöffler M, Muller H G, Dörner R and Keller U 2008 Attosecond angular streaking *Nat. Phys.* **4** 565
[3] Landsman A S and Keller U 2015 Attosecond science and the tunnelling time problem *Phys. Rep.* **547** 1
[4] Hofmann C, Landsman A S and Keller U 2019 Attoclock revisited on electron tunnelling time *J. Mod. Opt.* **66** 1052
[5] Kheifets A S 2020 The attoclock and the tunneling time debate *J. Phys. B: At. Mol. Opt. Phys.* **53** 072001
[6] Satya Sainadh U, Sang R T and Litvinyuk I V 2020 Attoclock and the quest for tunnelling time in strong-field physics *J. Phys. Photon.* **2** 042002
[7] Hofmann C, Bray A, Koch W, Ni H and Shvetsov-Shilovski N I 2021 Quantum battles in attoscience: tunnelling *Eur. Phys. J.* D **75** 208
[8] Torlina L *et al* 2015 Interpreting attoclock measurements of tunnelling times *Nat. Phys.* **11** 503
[9] Ni H, Saalmann U and Rost J M 2016 Tunneling ionization time resolved by backpropagation *Phys. Rev. Lett.* **117** 023002
[10] Han M *et al* 2019 Unifying tunneling pictures of strong-field ionization with an improved attoclock *Phys. Rev. Lett.* **123** 073201
[11] Sainadh U S *et al* 2019 Attosecond angular streaking and tunnelling time in atomic hydrogen *Nature* **568** 75
[12] Serov V V, Bray A W and Kheifets A S 2019 Numerical attoclock on atomic and molecular hydrogen *Phys. Rev.* A **99** 063428
[13] Eicke N and Lein M 2019 Attoclock with counter-rotating bicircular laser fields *Phys. Rev.* A **99** 031402
[14] Yuan M H and Bian X B 2020 Angular distribution of photoelectron momentum in above-threshold ionization by circularly polarized laser pulses *Phys. Rev.* A **101** 013412
[15] Serov V V, Cesca J and Kheifets A S 2021 Numerical and laboratory attoclock simulations on nobel-gas atoms *Phys. Rev.* A **103** 023110

[16] Klaiber M, Yakaboylu E, Bauke H, Hatsagortsyan K Z and Keitel C H 2013 Under-the-barrier dynamics in laser-induced relativistic tunneling *Phys. Rev. Lett.* **110** 153004
[17] Eckart S *et al* 2018 Direct experimental access to the nonadiabatic initial momentum offset upon tunnel ionization *Phys. Rev. Lett.* **121** 163202
[18] Liu K *et al* 2019 Detecting and characterizing the nonadiabaticity of laser-induced quantum tunneling *Phys. Rev. Lett.* **122** 053202
[19] Barth I and Smirnova O 2011 Nonadiabatic tunneling in circularly polarized laser fields: physical picture and calculations *Phys. Rev.* A **84** 063415
[20] Liu K, Ni H, Renziehausen K, Rost J-M and Barth I 2018 Deformation of atomic $p_{\pm}$ orbitals in strong elliptically polarized laser fields: ionization time drifts and spatial photoelectron separation *Phys. Rev. Lett.* **121** 203201
[21] Ni H *et al* 2020 Theory of subcycle linear momentum transfer in strong-field tunneling ionization *Phys. Rev. Lett.* **125** 073202
[22] Ni H, Saalmann U and Rost J M 2018 Tunneling exit characteristics from classical backpropagation of an ionized electron wave packet *Phys. Rev.* A **97** 013426
[23] Ni H, Eicke N, Ruiz C, Cai J, Oppermann F, Shvetsov-Shilovski N I and Pi L W 2018 Tunneling criteria and a nonadiabatic term for strong-field ionization *Phys. Rev.* A **98** 013411
[24] Smeenk C T L, Arissian L, Zhou B, Mysyrowicz A, Villeneuve D M, Staudte A and Corkum P B 2011 Partitioning of the linear photon momentum in multiphoton ionization *Phys. Rev. Lett.* **106** 193002
[25] Willenberg B, Maurer J, Mayer B W and Keller U 2019 Sub-cycle time resolution of multi-photon momentum transfer in strong-field ionization *Nat. Commun.* **10** 5548
[26] Li M, Geng J-W, Liu H, Deng Y, Wu C, Peng L-Y, Gong Q and Liu Y 2014 Classical-quantum correspondence for above-threshold ionization *Phys. Rev. Lett.* **112** 113002
[27] Shvetsov-Shilovski N I *et al* 2016 Semiclassical two-step model for strong-field ionization *Phys. Rev.* A **94** 013415
[28] Shannon C E 1948 A mathematical theory of communication *Bell Syst. Tech. J.* **27** 379
[29] Ivanov I A, Nam C H and Kim K T 2019 Entropy-based view of the strong field ionization process *J. Phys. B: At. Mol. Opt. Phys.* **52** 085601
[30] Kullback S and Leibler R A 1951 On information and sufficiency *Ann. Math. Stat.* **22** 79
[31] Lein M, Gross E K U and Engel V 2020 Intense-field double ionization of helium: identifying the mechanism *Phys. Rev. Lett.* **85** 4707
[32] Tong X M, Hino K and Toshima N 2006 Phase-dependent atomic ionization in few-cycle intense laser fields *Phys. Rev.* A **74** 031405(R)
[33] Shvetsov-Shilovski N I, Dimitrovski D and Madsen L B 2012 Ionization in elliptically polarized pulses: multielectron polarization effects and asymmetry of photoelectron momentum distributions *Phys. Rev.* A **85** 023428
[34] Popruzhenko S V 2014 Keldysh theory of strong field ionization: history, applications, difficulties and perspectives *J. Phys. B: At. Mol. Opt. Phys.* **47** 204001
[35] Amini K *et al* 2019 Symphony on strong field approximation *Rep. Prog. Phys.* **82** 116001
[36] Figueira De Morrison Faria C, Schomerus H and Becker W 2002 High-order above-threshold ionization: the uniform approximation and the effect of the binding potential *Phys. Rev.* A **66** 043413
[37] Nayak A *et al* 2019 Saddle point approaches in strong field physics and generation of attosecond pulses *Phys. Rep.* **833** 1
[38] Jasarevic A *et al* 2020 Application of the saddle-point method to strong-laser-field ionization *J. Phys.* A **53** 125201
[39] Gribakin G F and Kuchiev M Y 1997 Multiphoton detachment of electrons from negative ions *Phys. Rev.* A **55** 3760
[40] Kjeldsen T K and Madsen L B 2006 Strong-field ionization of atoms and molecules: the two-term saddle-point method *Phys. Rev.* A **74** 023407
[41] Milosevic D B, Paulus G G, Bauer D and Becker W 2006 Above-threshold ionization by few-cycle pulses *J. Phys.* B **39** R203
[42] Frolov M V, Manakov N L, Minina A A, Popruzhenko S V and Starace A F 2017 Adiabatic-limit Coulomb factors for photoelectron and high-order-harmonic spectra *Phys. Rev.* A **96** 023406
[43] Ammosov M V, Delone N B and Krainov V P 1986 Tunnel ionization of complex atoms and of atomic ions in an alternating electromagnetic field *Sov. Phys. JETP* **64** 1191
[44] Delone N B and Krainov V P 1998 Tunneling and barrier-suppression ionization of atoms and ions in a laser radiation field *Phys.-Usp.* **41** 469
[45] Ivanov M Y, Spanner M and Smirnova O 2005 Anatomy of strong field ionization *J. Mod. Opt.* **52** 165
[46] Eicke N, Brennecke S and Lein M 2020 Attosecond-scale streaking methods for strong-field ionization by tailored fields *Phys. Rev. Lett.* **124** 043202
[47] Popruzhenko S and Bauer D 2008 Strong field approximation for systems with Coulomb interaction *Journal of Modern Optics* **55** 2573–89
[48] Yan T, Popruzhenko S V, Vrakking M J and Bauer D 2010 Low-Energy Structures in Strong Field Ionization Revealed by Quantum Orbits *Phys. Rev. Lett.* **105** 253002
[49] Yan T and Bauer D 2012 Sub-barrier Coulomb effects on the interference pattern in tunneling-ionization photoelectron spectra *Phys. Rev.* A **86** 053403